Alma Mater Studiorum Università di Bologna
Archivio istituzionale della ricerca

Coupled global and PIC modelling of the REGULUS cathode-less plasma thrusters operating on xenon, iodine and krypton

(Article begins on next page)

23 December 2024

Coupled Global and PIC Modelling of the REGULUS Cathode-less Plasma Thrusters Operating on Xenon, Iodine and Krypton

Shaun Andrews[a], Raoul Andriulli[a], Nabil Souhair[a], Simone Di Fede[b], Daniele Pavarin[c], Fabrizio Ponti[a], Mirko Magarotto[d]

[a]*Alma Propulsion Laboratory, University of Bologna, via Fontanelle 40, Forlì, 47121, Italy*
[b]*Centre of Studies and Activities for Space "G. Colombo" (CISAS), Univeristy of Padova, via Venezia 15, Padova, 352131, Italy*
[c]*Technology for Propulsion & Innovation (T4i) S.p.A., via Emilia 15, Monselice, 35043, Italy*
[d]*Department of Information Engineering (DEI), University of Padova, via Gradenigo 6/b, Padova, 35131, Italy*

Abstract

In recent years, the increasing demand for simple and low-cost propulsion for small satellites has given rise to a growing interest in low-power cathode-less plasma thrusters. Plasma is produced within a source tube using radiofrequency (RF) ionisation, enhanced by a magnetic field which also accelerates the discharge via the magnetic nozzle effect. A key advantage of cathode-less thrusters is that they can operate on a wider range of propellants, more easily stored, and often inexpensive (e.g., iodine) compared to traditional xenon. Despite simple hardware, plasma dynamics in this kind of device are highly complex. This work presents a numerical suite developed for cathode-less plasma thruster design and analysis. First, a 0D Global Source Model provides the plasma production in the source. A fully kinetic Particle-in-Cell model (2D and 3D) then handles plasma expansion in the magnetic nozzle. The capabilities of the suite are presented by-way-of investigation into the behaviour of alternative propellants iodine and krypton within the 50 and 150 W class REGULUS thrusters. The performance of each propellant is assessed in terms of plasma source and magnetic nozzle efficiencies. The results are then benchmarked against experimental measurements, obtaining agreement of <30%. At absorbed powers < 20 W, iodine exhibits comparable performance to xenon but produces about 50% less thrust as the power is increased above 40 W. This occurs because of the molecular reaction processes seen by iodine, and associated inelastic energy thresholds which result in higher collisional energy losses. The high ionisation energy of krypton results in a low source efficiency. Instead, in the magnetic nozzle, krypton was found to perform best, facilitating the most thermal-to-kinetic conversion. But, the final thrust is <20% of xenon; instead iodine performs within 43% of the thrust provided by xenon. Finally, iodine contamination of spacecraft surfaces are found to be comparable to estimates found in other electric propulsion devices.

Keywords: Helicon plasma thruster, Particle-in-Cell, Magnetic nozzle, Iodine, Krypton, Xenon, Global model

*Corresponding author
Email address:* sa15339@my.bristol.ac.uk (Shaun Andrews)

1. Introduction

Xenon has long been the almost-exclusive propellant choice for electric propulsion (EP); it has a low ionisation threshold (12.1 eV), high ionisation cross-section, is a heavy substance (131.3 AMU), and is chemically inert. However, Xe is a trace gas in the atmosphere ($<$0.1 ppm) and its limited production, as a by-product of air separation, is an expensive process (1800-5000 US\$/kg). As the EP market continues to grow, the current supply of Xe will be incapable of satisfying forecasted demand within 10 years [1, 2].

Potential alternative propellants are therefore a topic of current interest [3, 4]. Other noble gases, notably krypton [5], have been considered. Kr is more abundant (about 1 ppm) than Xe in the atmosphere and can be more than 10-times cheaper (290 US\$/kg). But Kr has an undesirably high ionisation threshold (14 eV) and low atomic mass (83.8 AMU), resulting in a lower thrust-to-power ratio, potentially outweighing the benefit of reduced cost. The storage density of Kr is also approximately 3-times less than that of Xe, which increases propellant tank volume and mass requirements.

Of particular interest is iodine [6–8], which is much more abundant (0.46 ppm of Earth's crustal rocks [9]) and less expensive (30 US\$/kg) than Xe. It can be stored unpressurised in its solid state at ambient conditions, presenting no transportation challenges due to the absence of pressurised cryogenic tanks. Both atomic and diatomic iodine also have a lower ionisation threshold (10.5 and 9.3 eV respectively) than Xe, and diatomic iodine has a relative mass (253.8 AMU) that is almost twice that of Xe [10].

But, although appealing, iodine is reactive, and its use in conventional Hall Effect Thrusters (HET) limited owing to cathode erosion [6]. Using iodine creates unique design and operational challenges. Iodine has a high electronegativity that can lead to corrosion with most common materials. In this respect, cathode-less thrusters under development, such as the Electron Cyclotron Resonance Thruster (ECRT) [11] and the radiofrequency (RF) plasma thruster— which includes the Helicon Plasma Thruster (HPT)— [12, 13] are superior and have been tested with a variety of propellants [14]. In the latter, plasma is produced by electron impact ionisation using an inductive RF antenna, enhanced by a magnetic field which also accelerates the discharge via the magnetic nozzle (MN) effect. Solid iodine has already been successfully tested in-orbit in systems such as the NPT30 RF ion thruster of ThrustMe [15] and T4i S.p.A.'s REGULUS-50 RF thruster in Q1 2021 [16]. It is complete also to mention water as a promising candidate [2, 17], which is highly abundant, as well as atmosphere-breathing concepts (O, N_2) [18–20].

The simulation of atomic propellants, mainly xenon, is very well established. This has included global [21–23], fluid [24–26], kinetic [27], Particle-in-Cell with Monte-Carlo Collisions (PIC-MCC) [28, 29] and hybrid-PIC [30] approaches. Increasing development is being made for the detailed chemistry of excited species [31], including the sensitivity of different data-sets of cross-sections (up to 30% on source electron density). This has been applied to both global models and multidimensional fluid and hybrid codes, yielding improved experimental agree-

2

ment for both Xe and Kr [31].

However, because of the more complex reaction processes and energy-loss mechanisms in molecular plasmas— as well as the historical lack of reliable collision cross-section data— modelling the complex chemistry of alternative propellants in cathode-less thrusters is in its early stages. Models must be capable of handling mixtures of several substances in addition to molecular collisions such as dissociation, vibrational and rotational excitations. So far, this has been limited to global models, which have predicted similar performance for both iodine and xenon under similar operating conditions [21–23]. More recently— and with newly calculated theoretical cross-sections— a global model of iodine by Lafleur et al. has also shown reasonable agreement with experimental measurements of an RF ion thruster [32]. In the same work, both the model and experiment showed also that the use of iodine can lead to a performance enhancement when compared with xenon for very-low RF powers < 20 W.

Coupling a PIC simulation of the MN in a HPT to a similar global model, the results of Souhair et al. [8, 20] also fell within the uncertainty of experimental thrust. Beyond global models, limited iodine chemistry has also been considered in hybrid-PIC plume models of other EP systems [33, 34]; while including heavy-species collisions, molecular chemistry and inelastic processes were absent. Sheppard and Little [17] developed a semi-empirical 1D model to characterise the complex chemistry of water and Zhou et al. [35] have used a hybrid-PIC model to evaluate air mixtures in a HPT. It was found that electron heating was less effective for N_2 and O given the same amount of deposited power, yielding thrust efficiencies of 1.3-4.5%, which were noticeably worse than the 10.4% found for Xe.

This work presents the modelling of iodine and krypton as alternative propellant choices with a recently developed numerical suite for cathode-less plasma thrusters [36, 37]. A 0D Global Source Model (GSM) [20, 38] evaluates the properties of the discharge (a fluid model is also available but not applied in this specific work [24, 39, 40]), then a fully kinetic 2D PIC model considers the plasma expansion in the MN [28]. Interaction of the species with different types of surfaces (dielectric, metallic, etc.) and complex magnetic topologies can be modelled. Finally, a 3D PIC model is used to assess the plume interactions with non-axisymmetric spacecraft surfaces [29]. The suite can also handle multiple species; the core innovation in this work is that both the GSM and PIC model have been extended to handle collisions/chemistry typical of diatomic molecules (exampled by iodine). Further, specific innovations to the PIC model—including dielectric boundary conditions and secondary electron emission—are introduced also.

Simulations are performed for two different laboratory prototypes of cathode-less RF-based plasma thrusters under development at Technology for Propulsion and Innovation (T4i) S.p.A., derived from the commercial REGULUS-50 [7, 16] and REGULUS-150 [41], using krypton and iodine as propellant. The plasma profiles and propulsive performance are then studied and compared with xenon. The rest of the work is organized as follows: Section 2 describes the configuration of the REGULUS thruster and the structure of the numerical suite; section

3

3 compares the numerical propulsive estimates with experimental measures; section 4 discusses the plasma source performance; section 5 presents the results of the PIC simulations with 2D plasma profiles and MN performance; section 6 assesses the surface interaction of iodine with the 3D PIC code; section 7 gives the conclusions.
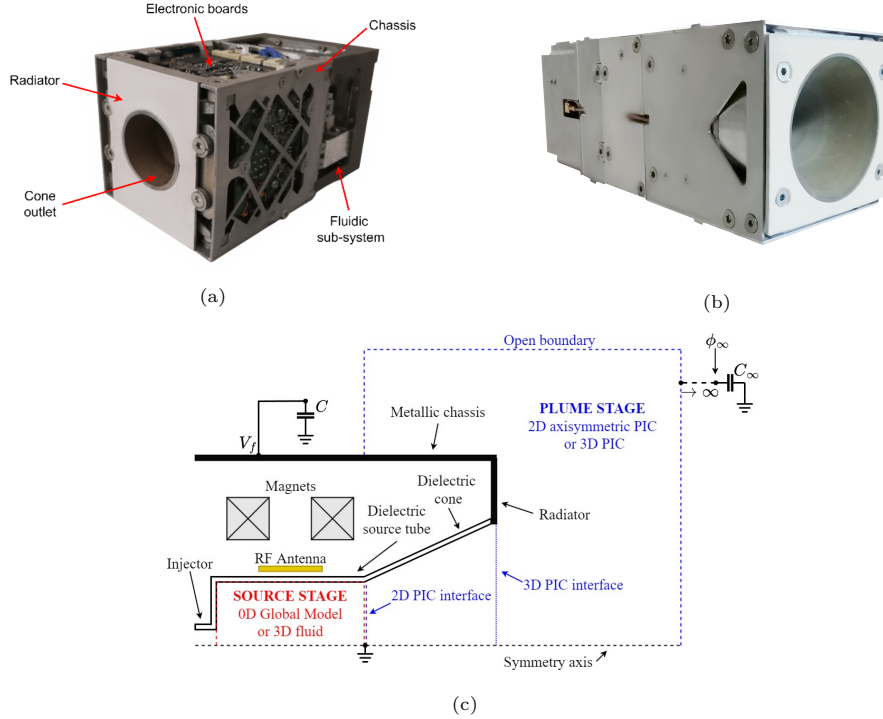

Figure 1: a) REGULUS-50-I_2; b) REGULUS-150-Xe; c) General REGULUS-type thruster schematic (not to scale)

2. Physical and numerical model

The aforementioned laboratory prototypes, derived from REGULUS-50 and REGULUS-150 (and hereby referred to as-such), are 50 W and 150 W class RF-based cathode-less plasma thrusters developed since 2015 at T4i S.p.A.; Figs. 1(a) and (b) show REGULUS-50-I_2 and REGULUS-150-Xe respectively. Fig. 1 (c) then sketches an arbitrary configuration of the REGULUS-type laboratory prototype, with an overview of the numerical approach. The source tube and expansion cone are hexagonal Boron Nitride (h-BN); the radiator and chassis structure are aluminium. An injector at the source tube base delivers a mass flow rate $\dot{m}$ of propellant, while the antenna emits power P_{RF}. Annular permanent magnets, concentric with the source tube, generate a convergent-divergent

4

magnetostatic field B. Due to the vast range in length and timescales over which plasma processes occur, the numerical suite simulates the thruster with a coupled multiscale structure [37].
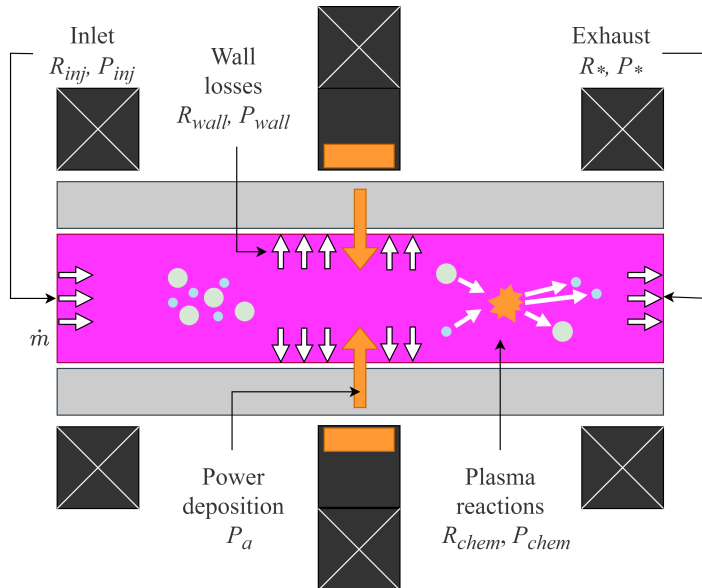

Figure 2: Schematic of the Global Source Model, with associated species flux and power terms.

The GSM considers the RF power deposition into the plasma and provides the discharge properties at the source tube exit. These properties then serve as inputs to the 2D PIC code [28], which models the plasma transport in the expansion cone and MN. This provides the propulsive performance estimates (i.e., thrust and efficiency). Finally, the 3D PIC code [29] is used to analyse the plume-surface interactions with non-axisymmetric spacecraft.

2.1. Global Source Model

A volume-averaged 0D Global Source Model (GSM) is used to obtain the properties of the plasma discharge within the source tube [20, 31, 32, 38, 42]. The GSM allows efficient assessment of chemical models and has trivial computational cost (compared to multi-dimensional fluid or hybrid solvers), while providing reasonable precision in the estimate of discharge and propulsive properties [20, 31, 32, 38, 42].

The plasma production is assumed to occur only within the cylindrical region of the source tube, with an open end for the outlet, defined in Fig. 2; it has radius $\mathcal{R}$, length $\mathcal{L}$ and volume $\mathcal{V} = \pi\mathcal{R}^2\mathcal{L}$. The magnetic field is considered uniform and perfectly aligned with the thruster axis; the effect of cusps is accounted for through empirical relations [31, 38]. The GSM then effectively considers a singular node to compute the bulk properties for each species. The

spatial non-uniformity in the plasma properties, induced by the magnetic confinement, is then accounted through semi-heuristic sheath-to-bulk edge ratios for low-pressure plasma [20, 32, 42]. The particle flux balance —for a general species k— and electron power balance respectively are solved as [32]:

$$\frac{dn_k}{dt} = R^k_{chem} - R^k_{wall} + R^k_{inj} - R^k_* \tag{1}$$

$$\frac{d}{dt}\left(\frac{3}{2}n_e\langle T_e\rangle\right) = P'''_a - P'''_{chem} - P'''_{wall} + P'''_{inj} - P'''_*, \tag{2}$$

where n_k is the bulk number density of the kth species, and $\langle T_e\rangle$ is the volume-averaged electron temperature. Heavy species are assumed cold and isothermal [31]. In Eq. 1, the terms correspond to the production/loss of the kth species due to chemical reactions R^k_{chem}; the loss/production of the species due to wall interactions R^k_{wall}; the injection of the propellant gas into the source tube R^k_{inj}; and the losses exiting the outlet into the MN R^k_*:

$$R^k_{chem} = \sum_j K_{jk}n_j n_e - \sum_j K_{kj}n_k n_e, \tag{3}$$

$$R^k_{wall} = \frac{S^k}{\mathcal{V}}\Gamma^k_{wall}, \tag{4}$$

$$R^k_{inj} = \frac{\dot{m}_k}{m_k\mathcal{V}}, \tag{5}$$

$$R^k_* = \frac{\pi\mathcal{R}^2}{\mathcal{V}}h^k_L\beta^k\Gamma^k_*, \tag{6}$$

where K_{kj} is the reaction rate coefficient, given later in section 2.3, with kj referring to the reactant k and the product j; m_k and $\dot{m}_k$ are the mass and mass flow rate of the species k. The total effective surface loss areas at the lateral and back walls S_k is computed according to empirical relations for either electropositive atomic or electronegative molecular plasma [20, 38, 42]. For a closed cylinder with a non-uniform magnetic field (i.e., with cusps), it can be expressed as

$$S^k = 2\pi\mathcal{R}^2 h^k_L\beta^k + h^k_{R\perp}\left(2\pi\mathcal{R}\mathcal{L} - S_{cusp}\right) + h^k_{R||}S_{cusp}, \tag{7}$$

where $S_{cusp} = 4N_{cusp}\sqrt{r_{ci}r_{ce}}2\pi\mathcal{R}$ is the equivalent area influenced by magnetic cusps [38]; N_{cusp} is the number of cusps present in the magnetic topology, and r_{ci} and r_{ce} are the ion and electron cyclotron radii. The terms $h_{R||,\perp}$, h_L and β are semi-heuristic coefficients that account for the non-uniformity of the plasma profiles inside the source tube, and for the effect of electronegativity on the diffusion coefficients [20, 32, 38, 42]. They are the radial sheath-to-bulk density ratio, axial sheath-to-bulk density ratio, and radially-averaged-to-bulk density ratio respectively; these are expressed as [20, 42]:

$$h^k_{R||} = 0.8\left(4 + \frac{\mathcal{R}}{\lambda_k} + (1+\alpha_-)^{1/2}\gamma_+\left(\frac{\mathcal{R}}{\lambda_k}\right)^2\right)^{-1/2}\left(\frac{\gamma_- - 1}{\gamma_-(1+\alpha_-)^2} + \frac{1}{\gamma_-}\right)^{1/2}, \tag{8}$$

$$h_{R\perp}^k = \left(1 + (\omega_{ck}\tau_k)^2\right)^{-1} h_{R||}^k, \tag{9}$$

$$h_L^k = 0.86 \left(3 + \frac{\mathcal{L}}{2\lambda_k} + (1 + \alpha_-)^{1/2}\frac{\gamma_+}{5}\left(\frac{\mathcal{L}}{\lambda_k}\right)^2\right)^{-1/2}\left(\frac{\gamma_- - 1}{\gamma_-(1 + \alpha_-)^2} + \frac{1}{\gamma_-}\right)^{1/2}, \tag{10}$$

$$\beta^k = \frac{1}{\left(1 - h_{R\perp}^{1/6}\right)}\left(\left[\left(1 - h_{R\perp}^{1/6}\right) - 1\right]^7 + 1\right), \tag{11}$$

where $\alpha_- = n_-/n_e$ is the bulk electronegativity ratio; $\gamma_+ = T_+/T_e$ and $\gamma_- = T_e/T_-$ are the positive ion-to-electron and electron-to-negative ion temperature ratios respectively [20, 42]; $\omega_{ck} = eB/m_k$ is the species cyclotron frequency, where e is the elementary charge; λ_k and τ_k are then the species mean free path and mean free time respectively, from the reaction rates K.

Regarding flux terms, Γ_{wall} is the species flux toward the lateral and back walls and $\Gamma_\star$ the equivalent term at the open outlet. For neutral species $k0$, electrons e and positive species $k+$, they are both expressed as:

$$\Gamma^{k0} = \frac{1}{4}n_{k0}\bar{v}_{k0}, \tag{12}$$

$$\Gamma^e = \frac{n_e\bar{v}_e}{4}exp\left(-\frac{\Delta\phi}{T_e}\right), \tag{13}$$

$$\Gamma^{k+} = n_{k+}u_B, \tag{14}$$

where $\bar{v}_k = \sqrt{8eT_k/\pi m_k}$ and $\Delta\phi$ is the sheath potential drop, which is defined later in this section. u_B is the Bohm speed, which, to account for electronegativity [42], is expressed as

$$u_{B_k} = \sqrt{\frac{eT_e}{m_k}}\left(\frac{1 + \alpha_-}{1 + \gamma_-\alpha_-}\right)^{1/2}. \tag{15}$$

Note that when the plasma is electropositive (i.e. xenon or krypton), Eq. 10 reduces to the standard Bohm speed [31]. Then, a current-free condition is enforced at the walls according to the Bohm sheath criterion,

$$\Gamma_{wall}^e = \sum_{k+}\left(\Gamma_{wall}^{k+}\right) = \sum_{k+}\left(n_{k+}u_{B_{k+}}\right). \tag{16}$$

Furthermore, each outward flux of positive ions, recombining at the wall, corresponds to an inward flux of neutral particles $\Gamma^{k0} = -\Gamma^{k+}$. Note here that, for iodine, a molecule of I_2 can be formed at half the rate at which an I atom sticks to a wall in a recombination reaction $2I \rightarrow I_2$; this is considered as $\Gamma_{I_2} = -\gamma_{rec}\Gamma_I$, where $\gamma_{rec} = 0.02$ is the recombination coefficient [42]. Regarding any negative ions, $\Gamma_{wall}^{k-} = 0$ [8].

Considering now the power balance of Eq. 2, the superscript $'''$ indicates the volume density of the generic power term $P''' = P/\mathcal{V}$. The terms correspond to the antenna RF power density absorbed into the plasma (a model input), the source/sink term related to the chemical reactions, the energy loss to the walls, the energy flux associated to the propellant flow injected into the source (taken as negligible hereafter), and the power exiting the source tube into the MN. These terms are evaluated as [32]:

$$P'''_{chem} = \sum_j K_{ij} n_j n_e \Delta U_{ij} + \sum_i K_{ij} n_i n_e \frac{3m_e}{m_i} \langle T_e \rangle, \tag{17}$$

$$P'''_{wall} = R^e_{wall} \left(2\langle T_e \rangle + \Delta\phi \right), \tag{18}$$

$$P'''_* = R^e_* \left(2\langle T_e \rangle + \Delta\phi \right), \tag{19}$$

where ΔU is the energy gap of the reaction process, the values for which are given in section 2.3. Regarding Eqs. 14 and 15, the $2\langle T_e \rangle$ term is the electron kinetic energy lost at the surface, found by computing the average energy flux along one axis for a Maxwellian [42]. The (positive) ion kinetic energy lost corresponds to the energy acquired by the ions to enter the sheath, and the energy acquired during the acceleration in the sheath; the potential drop can then be decomposed into the absolute value of the sheath voltage V_s and V_p the plasma potential, adapted to electronegative plasmas as [42],

$$\Delta\phi = V_s + V_p, \tag{20}$$

$$V_s = \langle T_e \rangle ln \left(\frac{4}{\bar{v}_e} \frac{\sum_{k+} n_{k+} u_{B_{k+}}}{\sum_{k+} n_{k+}} \frac{1 + \alpha_-}{1 + \alpha_-(\bar{v}_-/\bar{v}_e)^2} \right), \tag{21}$$

$$V_p = \frac{\langle T_e \rangle}{2} \frac{1 + \alpha_-}{1 + \gamma_- \alpha_-}. \tag{22}$$

With an electropositive plasma, the total energy loss reduces to the classical expression,

$$2\langle T_e \rangle + \Delta\phi = \langle T_e \rangle \left(\frac{5}{2} + \frac{1}{2} ln \left(\frac{2\pi m_e}{m_{k+}} \right) \right). \tag{23}$$

Finally, the electronegativity at the sheath edge as a function of electronegativity in the plasma bulk is solved numerically as [42],

$$\alpha_- = \frac{n_{k-}}{n_e} exp \left(\frac{V_p}{\langle T_e \rangle} (1 - \gamma_-) \right). \tag{24}$$

Once the GSM establishes a solution, the discharge properties at the source tube outlet, required as input to the PIC model, are then obtained as

$$n_{k*} = n_k \beta_k h_L^k, \tag{25}$$

$$\dot{m}_{k*} = m_k n_k \beta_k h_L^k u_{B_k} \pi \mathcal{R}^2, \tag{26}$$

$$T_{e*} \equiv \langle T_e \rangle, \tag{27}$$

where n_{k*}, $\dot{m}_{k*}$ and T_{e*} become the PIC-injected number density, mass flow rate and electron temperature respectively.

8

2.2. Particle-in-Cell

A two-dimensional axisymmetric Particle-in-Cell (PIC) code with Direct Simulation Monte-Carlo (DSMC) collisions is used to consider the plasma transport in the expansion cone and MN [28, 43]. Macro-particle trajectories are integrated with the typical leap-frog Boris scheme [44]. The null collision method [45] performs collision interactions between macro-particles and a surface interaction module handles ion recombination, neutral accommodation, secondary electron emission, and dielectric surface charging.

The plasma potential ϕ is obtained from the general dielectric form of the Poisson's equation,

$$\nabla \cdot \left(\gamma^2 \varepsilon_r \varepsilon_0 \nabla \phi\right) = -\left(\rho + \varrho\right) \tag{28}$$

and is solved with a successive over-relaxation (SOR) Gauss-Seidel algorithm, where ε_0 is the vacuum permittivity, ε_r is a non-dimensional 'relative permittivity' that accounts for dielectric materials (3.2 for h-BN [46]), ρ and ϱ are the volumetric plasma and volumetric surface charge densities respectively, and γ is a global permittivity scaling for the purposes of numerical acceleration [6].

2.2.1. Boundary conditions

According to the boundaries shown in Fig. 2 (c), the source tube exit is given the reference potential $\phi_0 = 0$. The symmetry axis is a zero-Neumann, and remaining external boundaries are the non-stationary Robin condition introduced by Andrews et al. [28]. In practice, the thruster chassis is coated in a thin layer of insulating material; thus, it is considered to remain grounded to the free-space potential ϕ_∞ ($V_f = \phi_\infty$ and $C = 0$ in Fig. 1(c)). The dielectric cone is included in the mesh, and so is accounted for by the effect of its relative permittivity and surface charge according to Eq. 21. This allows a self-consistent local current-free condition on the dielectric surface. Particles are injected at the source tube exit with a one-sided Maxwellian distribution. Ions and neutrals reaching the external boundaries are removed, whereas electrons are selectively reflected according to whether they possess sufficient energy to escape the potential drop $e\phi_\infty$ [28]. All particles returning to the plasma source are removed and undergo full reflection on the symmetry axis. The free space potential ϕ_∞ is self-consistently updated to maintain a globally current-free plasma $\left(I_{k-} = -\sum_{k+} I_{k+}\right)$ to infinity, via a virtual capacitor C_∞ connecting ϕ_∞ to the total net current of all species leaving the open boundaries [28].

2.2.2. Surface interactions

On both metallic and dielectric surfaces, ions undergo recombination with a thermal accommodation coefficient [47] of $a_t = 0.6$, and neutrals diffusely reflect with $a_t = 0.9$. When electrons strike the dielectric surface, one of the following four events may occur [48]: (i) the incident electron is absorbed; (ii) it knocks out a secondary electron; (iii) it knocks out two secondary electrons; (iv) it is

9

elastically reflected. For electron energy E_e [eV]:

$$W_0(E_e) = C_0 \exp\left(-\frac{E_e^2}{E_0^2}\right) \tag{29}$$

$$W_r(E_e) = C_r \exp\left(-\frac{E_e^2}{E_r^2}\right) \tag{30}$$

$$W_2(E_e) = 1 - \exp\left(-\frac{E_e^2}{E_2^2}\right) \tag{31}$$

$$W_1(E_e) = 1 - W_0(E_e) - W_r(E_e) - W_2(E_e) \tag{32}$$

where $W_0(E_e)$, $W_r(E_e)$, $W_2(E_e)$, and $W_1(E_e)$ are the probabilities for the incident electron to be absorbed, to be elastically reflected, to yield two true secondary electrons, and to yield one true secondary electron, respectively. For h-BN, the coefficients are $C_0 = 0.5$, $E_0 = 43.5$ eV, $C_r = 0.5$, $E_r = 30$ eV and $E_2 = 127.9$ eV [49]. The initial velocity distribution of the true secondary electrons is a diffuse cosine, with $a_t = 0.6$, and the most probable speed is calculated with a secondary electron temperature $T_{SEE} = T_e/3$, where T_e is the local electron temperature. Finally, the charge of recombined ions and absorbed electrons is added to the accumulating surface charge ϱ by scattering the macro-particle charge to the nearest mesh node (the wall is resolved to a Debye length), using a Ruyten shape factor [43]. In this way, surface charge is treated as an accumulation of static frozen macro-particles.

2.2.3. 3D PIC

The 3D code follows the same formulation as described for the 2D code, although it is Cartesian, uses an unstructured tetrahedral mesh and its domain extended (there is also no symmetric boundary condition in the 3D code). A capacitive charging circuit is also established to the spacecraft surfaces. Full details of the 3D model can be found in references [29, 37].

2.3. Collisions and chemistry

The modelling of atomic substances (Xe and Kr) is common and well-known [21–23, 25, 26, 31], so the discussion here is focused on molecular iodine, which is the novel part implemented in the model. The lumping procedure for Xe and Kr, required to reduce the number of considered excitation states, is however discussed is section 2.3.3.

2.3.1. Iodine chemistry

The species present in the iodine discharge are molecular iodine I_2, atomic iodine I, singly-charged positive and negative atomic ions, namely I^+ and I^-, and positive molecular iodine ions I_2^+. Double-charged ions and excited species other than I^* are not considered. Although the negative ions are not expected to be significant in population compared to positive ions, their influence may affect the diffusion process within the source tube [8]. Electron impact reactions and heavy species collisions considered in this work are listed in Table 1,

10

Table 1: Iodine chemistry considered in the model

Reaction	Reaction type	ΔU [eV]	Ref.
Electron impact I_2			
$I_2 + e \rightarrow I_2 + e$	Elastic scattering	$3T_e m_e / m_{I_2}$	[42]
$I_2 + e \rightarrow I_2^+ + 2e$	Ionisation	9.31	[42]
$I_2 + e \rightarrow 2I + e$	Dissociative attachment	$3T_e/2$	[42]
$I_2 + e \rightarrow I_2 + e$	Dissociation	1.567	[42]
$I_2 + e \rightarrow I^+ + I + 2e$	Dissociative ionisation	10.9	[42]
Electron impact I			
$I + e \rightarrow I + e$	Elastic scattering	$3T_e m_e / m_I$	[42]
$I + e \rightarrow I^* + e$	Excitation	0.95	[42]
$I + e \rightarrow I^+ + 2e$	Ionisation	11.6	[42]
Electron impact I_2^+			
$I_2^+ + e \rightarrow I^+ + I + e$	Dissociation	2.1768	[42]
Detachment I_2^+			
$I^- + e \rightarrow I + 2e$	Detachment	4	[42]
Recombination			
$I^- + I_2^+ \rightarrow I + I_2$	Molecular recombination	-	[42]
$I^- + I^+ \rightarrow 2I$	Atomic recombination	-	[42]
Charge exchange			
$I_2 + I^+ \rightarrow I_2^+ + I$	Molecular-atomic	-	[33]
$I + I^+ \rightarrow I^+ + I$	Atomic	-	[33]
$I_2 + I_2^+ \rightarrow I_2^+ + I_2$	Molecular	-	[33]
Surface recombination			
$2I \rightarrow I_2$	Surface recombination	-	[42]

inclusive of the corresponding energy thresholds. An iodine molecule can disso-
ciate by electron impact through direct dissociation, dissociative ionisation or
attachment, with the latter being the principal source of negative ions. Nega-
tive ions can undergo detachment of the surplus electron by means of electron
impact. Atomic iodine, resulting from dissociation, can either elastically scatter
or ionise by electron impact producing atomic positive ions. Molecular iodine
can either scatter elastically against the electrons or ionise by electron impact
producing molecular ions, which can dissociate. Concerning heavy species col-

lisions, gas-phase recombination of positive and negative ions is considered, as well as charge-exchange. The surface recombination at the walls of atomic iodine into molecular iodine is considered also. Moreover, all species are subject to standard Coulomb collisions. Sources of the relevant cross-sections for iodine-electron chemistry, charge-exchange and Coulomb scattering can be found in references [42], [33] and [6] respectively. Considering the high number of species and reactions associated to iodine, the 14 levels of the fine structure have instead been grouped into one lumped level, given in Table 1. Finally, the PIC model includes an anomalous Bohm collisionality [50] via an equivalent frequency $\nu_B = \alpha_B \omega_{ce}$, where $\omega_{ce} = e|\mathbf{B}|/m_e$ is the electron cyclotron frequency and α_B is the Bohm coefficient.

2.3.2. Implementation

In the GSM, the reaction rates K involving electrons are calculated assuming a Maxwellian distribution of electron impact energy E_e

$$K(T_e) = \sqrt{\frac{8}{\pi m_e T_e^3}} \int_{\Delta U}^{\infty} E_e \sigma(E_e) e^{-E_e/T_e} dE_e \tag{33}$$

where σ is the collision cross-section [25, 51]. Regarding the heavy species collisions, i.e., recombination and charge exchange, the reaction rate is instead given by

$$K(T_1, T_2) = \int d^3 v_1 d^3 v_2 f_{v_1}(v_1) f_{v_2}(v_2) \sigma(|v_1 - v_2|)|v_1 - v_2| \tag{34}$$

where T_1, T_2 refer to the heavy species temperatures and v_1, v_2 the collision speed of the particles with distribution functions f_{v_1}, f_{v_2}. The PIC model instead uses collision cross sections directly in the DSMC method [28], which accounts for non-Maxwellian distributions. For ionisation, newly created ion macro-particles are given a velocity sampled from a Maxwellian about the local neutral fluid velocity. For dissociation, the same sampling is performed for each pair of new macro-particles, but the velocity is distributed uniformly and randomly over the pair.

2.3.3. Noble gas excitation lumping

Considering all excitation reactions (the fine-structure) leads to an unmanageable computational requirement, especially in the PIC model where many DSMC/MCC events per time-step would be necessary. Thus, a lumping procedure based on the assumption of local thermodynamic equilibrium is used, introduced in the previous work of Souhair et al. [31]. While the GSM completely accounts for each excited state in the flux and power balance, the PIC routine would further require too much computational power to track each excited species as macro-particles. Thus, the post-impact excited species are not modeled. Instead, it is presumed that excited neutrals immediately decay to the ground state, emitting radiation. As a result, the PIC excitation collisions
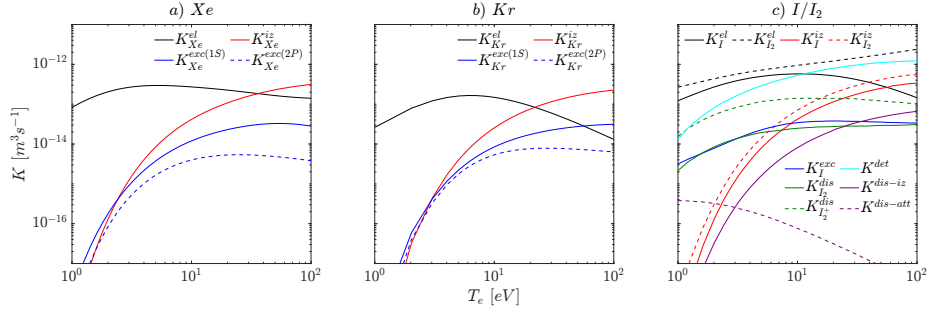
Figure 3: Maxwellian reaction rates of the alternative propellants: a) Xenon; b) Krypton; c) Iodine

behave as a pure electron energy sink. In Fig. 3, the reaction rates computed for the three gases analysed are reported assuming a Maxwellian distribution. In particular, for Xe and Kr, excited states have been lumped into 1S and 2P groups according to [31].

Table 2: Numerical setup parameters

Parameter			REGULUS-50	REGULUS-150
Source radius	$\mathcal{R}$	$[mm]$	6.5	8.5
Source length	$\mathcal{L}$	$[mm]$	90	100
Cone radius	$\mathcal{R}_{cone}$	$[mm]$	40	35
Cone length	$\mathcal{L}_{cone}$	$[mm]$	45	40
Mass flow rate	$\dot{m}$	$[mg/s]$	0.10	0.25
Input power	P_{in}	$[W]$	[15-60]	[50-185]
Cusps	N_{cusps}	$[-]$	2	2
Coupling efficiency	η_{RF}	$[-]$	0.85	0.70
System efficiency	η_{sys}	$[-]$	0.8	0.8
Background density	n_{back}	$[m^{-3}]$	2.42×10^{17}	
h-BN relative permittivity	ϵ_r	$[-]$	3.2	
Ion(neutral) accommodation	α_t	$[-]$	0.6(0.9)	
Recombination coefficient (I_2)	γ_{rec}	$[-]$	0.02	
Bohm coefficient	α_B	$[-]$	1/100	[1/100-1/16]
PIC mass scaling	f_M	$[-]$	250	
PIC permittivity scaling	γ	$[-]$	$\mathcal{R}/20\lambda_D$	
Virtual capacitance	C_∞	$[nF]$	0.8	
Origin cell size	$\Delta z_0, \Delta r_0$	$[mm]$	0.375	0.600
Boundary cell size	$\Delta z_b, \Delta r_b$	$[mm]$	3.0	4.8
Time-step	Δt	$[s]$	$0.5\Delta z_0/3v_{e,th}$	
Total (charged) macro-particles	N_p	$[-]$	$\approx 1.6 \times 10^6$	

3. Comparison to experiments

Measurements performed, for Xenon and Iodine, at the High Vacuum Facilities of the University of Padova are compared to the GSM+(2D)PIC model results. The experimental facility consists of a vacuum chamber of radius 0.3 m and length 2 m, maintained at a working pressure of 10^{-5} mbar. The propellant has been introduced in the source tube with $\dot{m}$ of 0.1 and 0.25 mg/s for REGULUS-50-Xe/I_2 [7, 13, 16] and REGULUS-150-Xe [41] respectively, through tailored fluidic subsystems. For iodine, this consists of a tank maintained at sublimation temperature by means of heaters to produce gas flow [16]. The thrusters are connected through a coaxial line to a power unit, consisting of a Spin HFPA-300 linear amplifier (1.8-30 MHz, power up to 300 W) driven by a HP 8648B signal generator. For REGULUS-50-Xe/I_2, the RF frequency was kept to 2 MHz, with the input power P_{in} in the range 15-60 W. For REGULUS-150-Xe, P_{in} was varied from 50-185 W. In the experiments the total power from the RF antenna P_{RF} was measured, the latter related to the absorbed power by $P_a = \eta_{RF} P_{RF}$, where η_{RF} is the coupling efficiency. From these same experiments [37], it was found that $\eta_{RF} = 0.85$ for REGULUS-50 and $\eta_{RF} = 0.7$ for REGULUS-150. The power consumed by the electronics is accounted for with the system efficiency $\eta_{sys} = P_{RF}/P_{in}$ and is about 0.8.

A thrust balance, tailored for small-to-medium size thrusters, was used to measure the performance [52]. The uncertainty associated to the thrust F is 15-20%, while the uncertainty associated to the power and mass flow rate are 10% and 10-15% respectively.

Regarding the numerical setup, the primary inputs to both the GSM and PIC model are listed in Table 2. For the PIC, the artificial permittivity scaling is set such that the source tube radius is resolved with 20 Debye lengths: $\gamma = \mathcal{R}/20\lambda_D$, where $\lambda_D = \sqrt{\epsilon_0 T_e/n_e e}$. This is because the ratio of the scaled Debye length to the system length scale ($\mathcal{R}$) must remain constant between simulations to preserve valid physical comparability. In the interest of repeatability, an example of input parameters for REGULUS-150-Xe have been provided in Table 3, including γ. The mass of heavy species is then reduced by a factor of 250 [28]. The resultant piece-wise-uniform mesh contains approximately 4000 cells, which increase in size towards the domain boundaries (while still resolving the local Debye length). The complete domain has dimensions of $20\mathcal{R} \times 10\mathcal{R}$. The time-step is such that it resolves the electron Courant-Friedrichs-Lewy (CFL) condition—$0.5\Delta z_0/3v_{e,th}$ with $v_{e,th} = \sqrt{2eT_e/m_e}$ the electron thermal speed—which was the limiting constraint in all cases, considering that the use of artificial permittivity also relaxes the plasma frequency constraint by a factor γ [28]. The virtual capacitance is the same as in previous studies [28, 37], that is $C_\infty = 0.8$ nF. A uniform neutral background density is then assumed from the ideal gas law at 10^{-5} mbar and 300 K.

Fig. 4 compares the measured thrust with the results of the GSM + (2D) PIC model (calculated per Appendix A). The numerical error bands arise from the uncertainty in collision cross sections, assumptions in the GSM, statistical variance in the PIC method, as well as uncertainty in η_{RF} and power consumed

14

Table 3: PIC inputs: REGULUS-150-Xe

P_{in} [W]	n_* [m^{-3}]	T_{e*} [eV]	γ
50	7.50×10^{17}	3.89	30
75	1.22×10^{18}	4.20	36
100	1.53×10^{18}	6.67	32
125	1.32×10^{18}	9.76	25
150	1.18×10^{18}	12.45	21
175	1.08×10^{18}	15.05	18

by electronics (η_{sys}); they are approximately 25%. It is prudent to state that the REGULUS-50 simulations used a constant Bohm parameter of $\alpha_B = 1/100$, whereas the results given for REGULUS-150 use a value that scales with the exhaust plasma wave energy ($\propto P_*$) [53]: P_* increases approximately from 1/100 to 1/16 with increasing P_*. There is excellent agreement in the case of REGULUS-150-Xe where, between 50-150 W, the experimental measures fall within the numerical uncertainty. However, the model begins to overestimate at higher power, with a maximum deviation of 33% at 160 W. Instead, the GSM+PIC describes the measured trend at higher powers for REGULUS-50-Xe well, but at 10-20 W underestimates by up to 28%. For REGULUS- 50-I2 the global trend is captured but underestimates the experiment by approximately 20% over the entire power range. Nonetheless, the GSM+PIC model reproduces the measures with sufficient accuracy. Potential sources of disagreement might be found in the precise estimate of chamber background density or vacuum chamber wall effects. Sensitivity of the PIC results to uncertain input parameters is discussed in Appendix B.

4. Source performance (GSM)

The effects on plasma production in the source tube are now analysed for xenon, krypton and iodine using the GSM. The REGULUS-150 thruster is considered at $\dot{m} = 0.25$ mg/s. To eliminate the influence of η_{RF}, results are given parametrically as a function of the absorbed power P_a between 10 and 150 W.

Fig. 5 (a) gives resultant peak ion density in the source tube. Kr^+ density closely trends Xe^+, both yielding about 5×10^{17} m^{-3} at 10 W. At 80 W however, Xe^+ density plateaus and steadily decreases approaching 150 W; Kr^+ continues increasing at the same rate. Regarding iodine, atomic ion production dominates the discharge; as the electron density increases with RF power, the dissociation rate becomes higher which enables the formation of I^+ and neutral I atoms, which can then undergo further electron impact ionisation. The ion production is much more efficient at lower power compared to the monoatomic propellants, but plateaus to similar densities as Kr^+ approaching 150 W. I_2^+ and I^- densities are 2 and 3 orders of magnitude less than I^+ respectively. The I_2^+ density remains relatively constant due to a combination of the higher electron density and higher dissociation rate coefficients caused by higher electron temperature
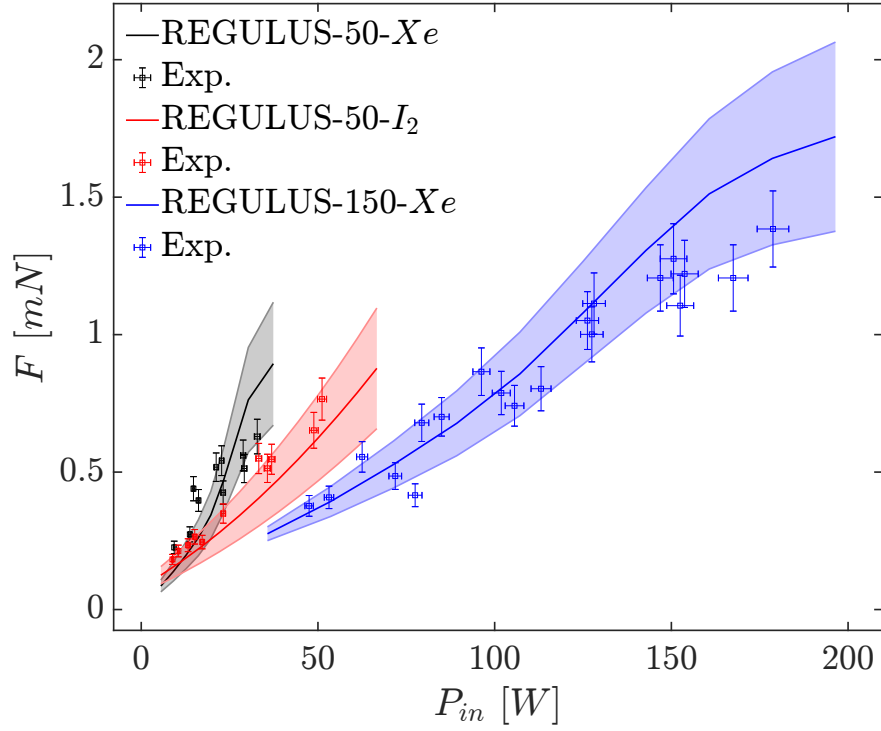
15

Figure 4: Comparison of thrust estimated from the GSM+(2D)PIC against experimental measures of REGULUS-50-Xe/I$_2$ and REGULUS-150-Xe as a function of the input power
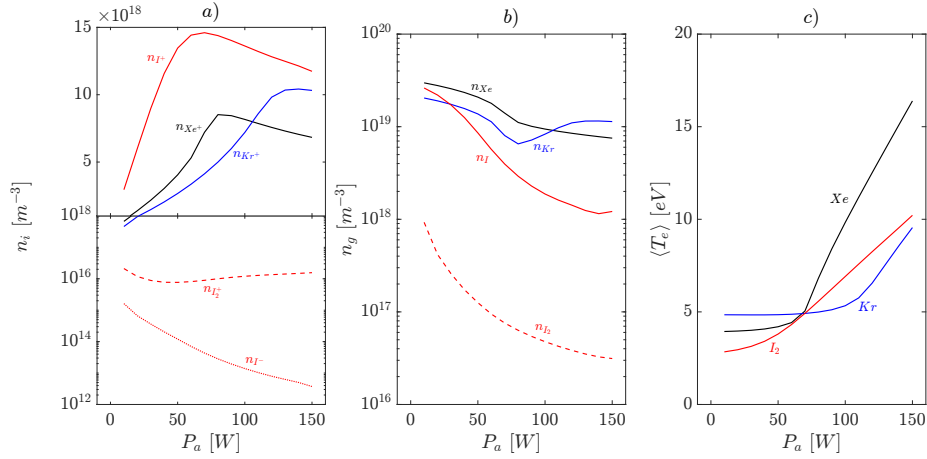

Figure 5: Plasma source properties as a function of absorbed power (REGULUS-150 at 0.25 mg/s): a) peak ion densities (note the transition from a logarithmic to linear scale at 1×10^{18}) b) neutral gas density; c) global-averaged electron temperature.
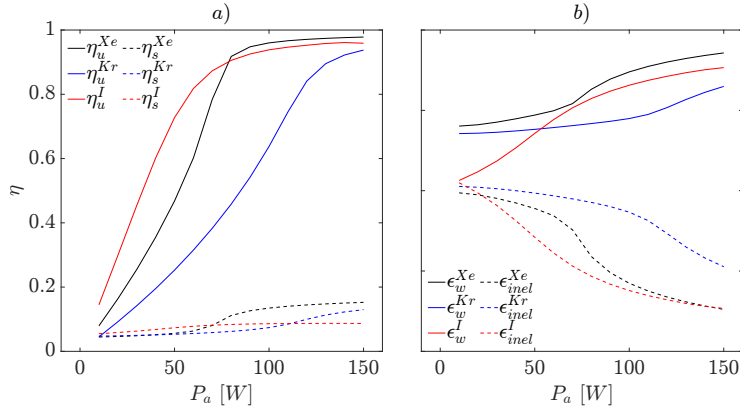
16

Figure 6: Plasma source performance (REGULUS-150 at 0.25 mg/s): a) Mass utilisation and source energy efficiencies; b) Wall loss and inelastic collision inefficiencies as a function of the absorbed power.

with increasing power, as well as the higher I_2 dissociation rate (which includes direct dissociation as well as dissociative ionization and dissociative attachment) and molecular iodine ionisation rate coefficient. The I^- density, and hence electronegativity, becomes increasingly negligible at high power. The decreasing I_2 density decreases the formation of negative ions from dissociative attachment, which are then also efficiently destroyed by electron impact recombination.

The corresponding neutral gas densities are given in Fig. 5 (b). Both Xe and I follow a general decrease as a result of depletion from ionisation. It is again noted that diatomic iodine gas I_2 is over 2 orders of magnitude less than the atomic. This depletion causes the electron temperature to rise which also increases the ionisation rate coefficient, further facilitating ion production. Instead, Kr density begins to increase at around 80 W.

The global electron temperature is given in Fig. 5 (c) and represents the amount of electron heating. All three curves follow a similar profile: a region of relatively constant temperature, followed by a transition to comparatively rapid increasing temperature at higher power. Once ion production becomes saturated, along with the power delivered for ionisation, the absorbed power instead heats electrons. Xe has a constant region of 4 eV until 50 W; Kr 4.8 eV until 90 W; iodine 2.8 eV until 20 W. This is explained by the relative ionisation energies of each species; 12.1, 14 and 10.5 eV respectively. The earlier increase for iodine is also partially a result of stronger neutral gas depletion due to more efficient ionisation. Since higher temperature yields more energy available for conversion in the MN, the electron heating is critical for thruster performance.

The source production performance is summarised by Figs. 6 (a) and (b), which show the relevant efficiencies and inefficiencies defined in Appendix A. The source efficiency η_s curves in Fig. 6 (a) correlate to the electron temperature trends. Iodine is seen to be the more robust propellant, with $\eta_s = 0.055 - 0.086$ consistent over the absorbed power range. Instead, both Xe and Kr perform

17

poorly at low power (< 0.047) but improve significantly once electron temperature increases. At 150 W, Xe and Kr have η_s of 0.15 and 0.13 respectively. Iodine outperforming xenon at low power agrees with several previous numerical and experimental studies [32, 42], and largely relates to the decreased excitation rate coefficient compared with the ionisation rate coefficient (see Fig. 3) as the electron temperature increases with increasing power. Fig. 6 (a) also shows mass utilisation efficiency η_u which, as expected, is overall greater for species with lower ionisation energies. As the power rises, η_u also rises because the ion beam current rises as a result of the increasing electron temperature (which raises the Bohm velocity) and positive ion densities. At 150 W, $\eta_u \approx 1$ for all propellants, but at lower power (<60 W), Kr and Xe exhibit much lower ionisation than iodine.

As per the power balance in the GSM, power not exhausted in the discharge is distributed via inelastic collisions and wall losses, the inefficiencies for which are given in Fig. 6 (b). Losses at the walls of the plasma source increase with power and are similar at high power. Iodine features significantly fewer (0.16 reduction compared to xenon) wall losses at low power, explaining partly its high source efficiency at these levels; this is because of iodine's low temperature at low power, reducing the energy loss to the wall per Eqs. 14-18. At low electron temperatures, both I and I_2 plasma loses more energy per electron-ion pair than xenon does (see Figs. 3 (a) and (c)), but this reverses at about 3–4 eV. This is caused by the various inelastic energy thresholds, reaction processes, and collision cross-sections. This explains why iodine sees up to an additional 0.05 collisional inefficiency at < 20 W compared to xenon, given the 2.8 and 4 eV electron temperatures respectively aforementioned in Fig. 5 (c). Once iodine's electron temperature rises above 3-4 eV at > 20 W, it's inefficiency yields up to a 0.15 improvement on xenon at 60-70 W. However, as Fig. 5 (c) shows, as the power is increased, the electron temperature with xenon increases at about twice the rate of iodine, and thus both inefficiencies approach 0.1 at 150 W. Fig. 6 (c) shows therefore that, if the electron temperature is high enough, operating iodine can result in fewer collisional energy losses. Kr experiences higher collisional losses than both Xe and iodine (up to about 0.1 further inefficiency at 150 W). This is because its temperature is generally higher, and η_u lower, which leads to a greater degree of collisionality.

5. Magnetic nozzle performance (2D PIC)

In this section, a laboratory version of REGULUS-50 is simulated for $\dot{m} = 0.1$ mg/s for P_a between 10 and 50 W.

5.1. 2D plasma profiles

The 2D spatial profiles are given for the case of $P_a = 50$ W; since the iodine discharge is dominated by atomic species, the profiles of molecular species and negative ions are not reported. Figs. 7 (a), (b) and (c) show the normalised neutral gas density for Xe, Kr and I respectively. The monoatomic gases show

18
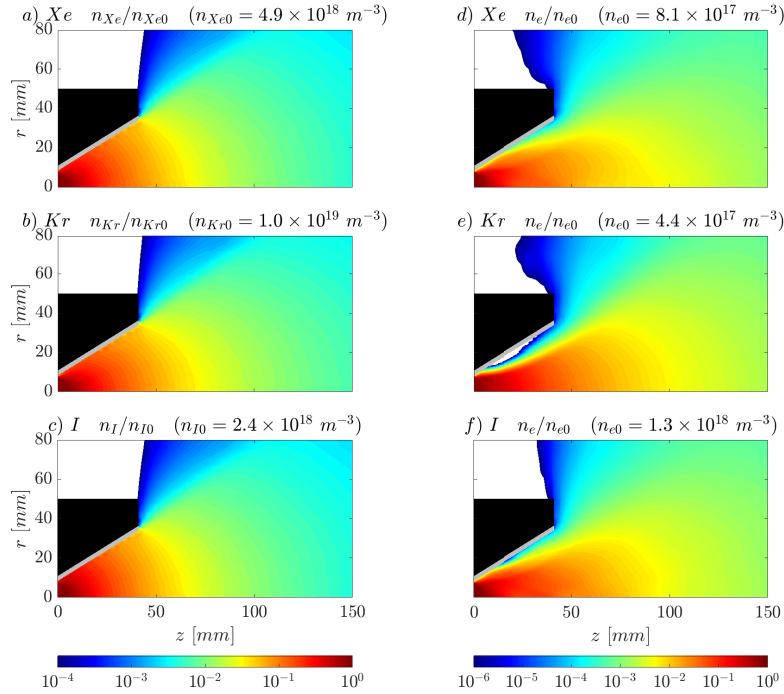
Figure 7: Normalised neutral gas density for a) Xenon n_{Xe}; Krypton n_{Kr}; c) Iodine n_I and electron density n_e for a) Xenon; b) Krypton; c) Iodine (REGULUS-50 at 0.1 mg/s).

nearly identical profiles, whereas there is a faster decay of I atoms downstream; the n_I density at the downstream boundary is 52% of n_{Xe}. This is because approximately 2% of atoms that strike the cone wall recombine instead to I_2. The in-plume ionisation for iodine is also about twice that of the atomic propellants, since its ionisation energy is lower at 10.5 eV. The expansion cone confines the neutral plume to improve the divergence efficiency and increase cold gas thrust. Figs. 7 (d), (e) and (f) show the normalised electron density for Xe, Kr and I. There is worse confinement for Xe and I due to the larger level of collisionality and their greater mass (they have more energy to escape the ambipolar confining electric field). The normalised plasma potential is thus given in Figs. 8 (a), (b) and (c). A sheath forms on the upstream section of the cone surface, which evolves into a reverse sheath (that is, the potential rises towards the wall) where the secondary ion expansion impacts the wall and electrons are shielded. This creates a potential peak on the wall that aids in ion confinement. For Kr and I, the peak has approximate strength of T_e compared to a much weaker peak with Xe. The peak for Kr forms earlier on the wall since its lighter mass means the secondary ion expansion is at a higher angle to the magnetic expansion.
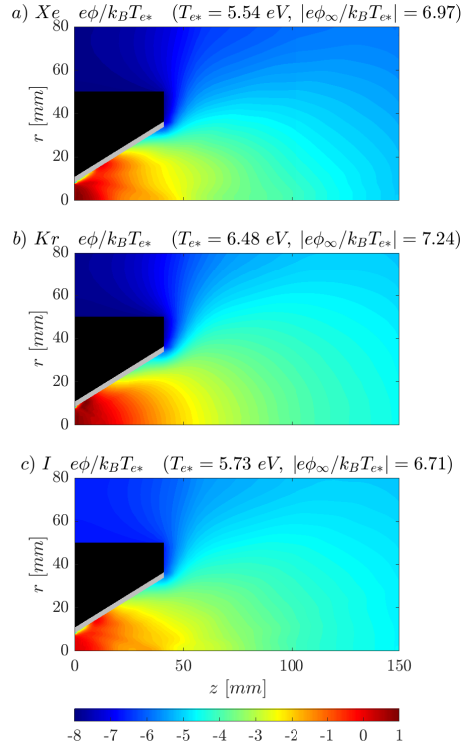
19

Figure 8: Normalised plasma potential $e\phi/k_B T_{e*}$ for a) Xenon; Krypton; c) Iodine (REGULUS-50 at 0.1 mg/s)
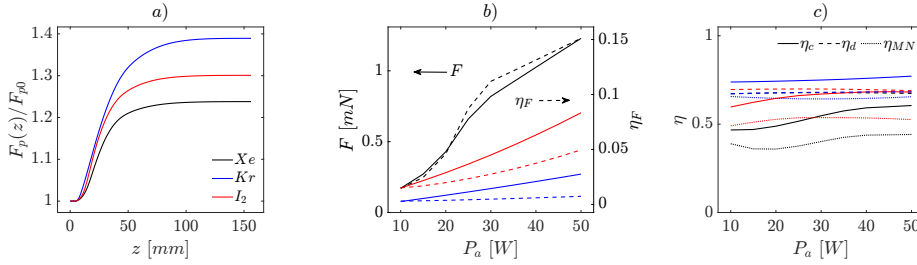

Figure 9: a) Plasma thrust gain in the magnetic nozzle as a function of the axial position; b) Thrust and thrust efficiency, as well as c) Magnetic nozzle efficiencies as a function of the absorbed power for REGULUS-50 at 0.1 mg/s.

5.2. Thrust and efficiencies

The plasma thrust gain of the 50 W cases presented above is given in Fig. 9. This excludes the neutral thrust to isolate the gain from the magnetic $j_{e\theta}B_r$ force (Eq. A1). Kr performs the best, with a gain of 1.39. I_2 and Xe yield gains of 1.3 and 1.24 respectively. This result is mainly driven by the discharge properties in the source. Kr has a greater discharge temperature at 6.48 eV, thus there is more

20

thermal energy conversion. The increased gain of iodine over xenon can instead be explained by the difference in collisionality; the neutral-to-plasma ratio is 1.85 and 6.05 for I and Xe respectively. The Xe plume has a greater degree of cross-field diffusion, demagnetising the plasma and inhibiting the formation of diamagnetic current. The MN gain however does not translate into absolute performance. Fig. 9 gives both the final thrust and thrust efficiency. Xenon is clearly the superior propellant, achieving $\eta_F = 0.15$ at 50 W compared to 0.05 and < 0.01 for iodine and krypton respectively. The plasma source though, is the main driving factor in propulsive performance.

To analyse the performance of each propellant in the MN in more detail, Fig. 9 (c) presents the conversion η_c, divergence η_d and MN efficiencies η_{MN} (defined in Appendix A). The conversion efficiency η_c of krypton is greatest, and is nearly constant, at approximately 0.75; for iodine, it increases from about 0.6 to a plateau beyond 30 W of 0.65; Xe yields the lowest average η_c increasing from 0.48 to 0.6. These trends can be explained by the previously-discussed result of discharge temperature, which limits the energy conversion in the MN according to the initial electron internal energy available from the production stage. The MN performance is clearly driven by this thermal-to-kinetic energy conversion, as η_d is near-constant for all three species, at around 0.65. At 50 W, η_{MN} is 0.64, 0.53 and 0.42 for krypton, iodine and xenon respectively. The larger power losses for iodine and xenon are due to losses at the cone wall (heavier species need stronger electric fields to turn their trajectories into the MN) and inelastic collisions in the plume.

6. Spacecraft interactions (3D PIC)

The 3D PIC code is utilised to assess the far-field plume interactions with spacecraft surfaces and determine spacecraft charging effects. Critically it can also capture the effects of non-axisymmetric spacecraft (from the potentials on those surfaces) on the plume dynamics. Fig. 10 shows the plume for REGULUS-50-Xe operating at 50 W within a 6U CubeSat ($200 \times 100 \times 300$ mm), a realistic mission configuration [54]. The spacecraft surface potential is assumed to begin equal to ϕ_∞, thus lower than the bulk plasma potential. This causes ions which have expanded beyond the confinement of the MN to reverse their flow direction and impinge on the front surface. The domain is a cylinder of radius 300 mm and length 600 mm, with origin 100 mm behind the thruster outlet.

The main concern is regarding iodine propellant and its potential corrosive action on spacecraft surfaces. Fig. 11 plots the particle flux on the front face of the 6U CubeSat for the three propellants. Based on these results, the highest neutral and ion particle fluxes on the spacecraft are approximately 4.1×10^{18} and 4.9×10^{18} m^{-2}s^{-1} respectively for iodine. Assuming all of the total incident particles stick to the surface and a constant rate of deposition per the profiles in Fig. 11, which is an extremely high conservative estimate, gives deposition per unit area of approximately 0.32 mg/cm^2 over the standard REGULUS-50 3000 Ns operation duration ($\sim$ 1500 hrs at 50 W). This is in-line with values reported in [33] for iodine HETs. However, not all iodine particles hitting the
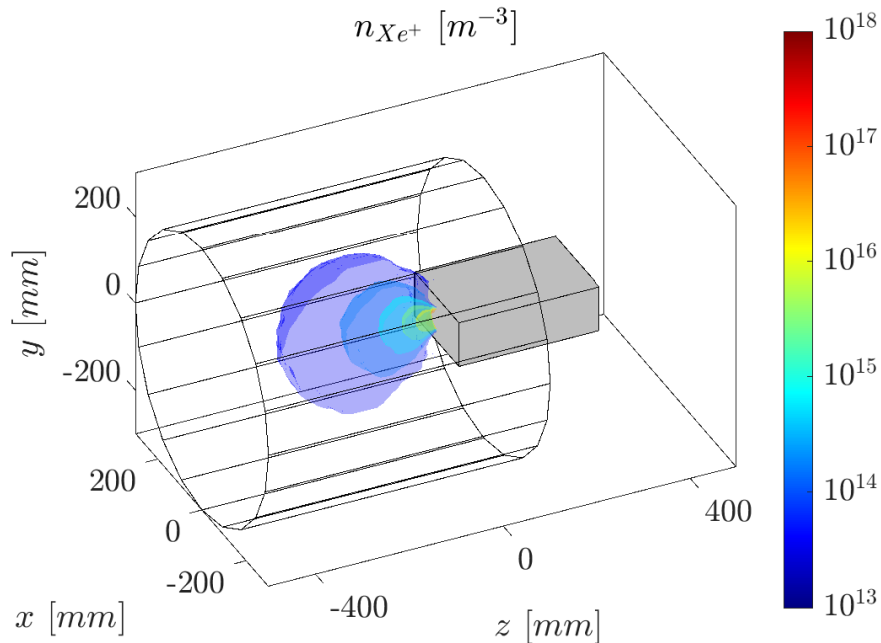
Figure 10: 3D contours of Xe ion density for REGULUS-50-Xe operating at $P_a = 50$ W in a 6U CubeSat. Plume has been cut in the y-plane for clarity. The computational domain is also shown.

surfaces will deposit or chemically react to the surface, given high vapor pressure of iodine at the temperature of a spacecraft in orbit ($\gtrsim 500$ K). The portion of particles that react to the surface will depend on the surface properties.

7. Conclusions

A numerical suite capable of simulating the propulsive performance and the plasma dynamics in a cathode-less plasma thruster has been presented. It consists of a 0D Global Source Model (GSM) for plasma production in the source tube, a 2D PIC code for the plasma expansion in the MN, and a 3D PIC code to assess spacecraft interactions and contamination. The results of the GSM coupled to the 2D PIC have been benchmarked against thrust measurements of the REGULUS-50 and REGULUS-150 laboratory prototypes. Overall, the model is in good agreement with experiment measurements, showing that the additional molecular iodine chemistry considered is quite reasonable and provides an acceptable level of accuracy <30%. The established xenon model largely falls within the experimental error for both thrusters. The model is therefore shown to be able to quantitatively and qualitatively reproduce system behaviour for variation in input power.

22

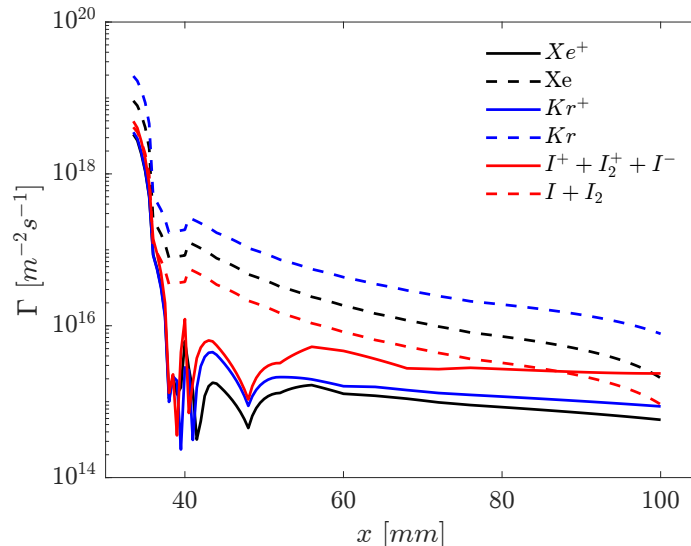Figure 11: Total neutral and ion particle fluxes on the surface of the CubeSat for REGULUS-50 at $P_a = 50$ W as a function of

Analysis of the plasma source reveals that, at $P_a < 50$ W, iodine is most efficient in terms of production. Lower overall collisional and wall energy losses are a result of the different collisional rate coefficients and inelastic energy thresholds for atomic and molecular iodine. Iodine can therefore have a lower average energy cost per ion produced and discharged than xenon. At higher powers however, xenon and krypton are superior. This is attributed to the mass utilisation and subsequent inelastic collision losses in the source tube. In the MN, krypton is found to be the most efficient in terms of thermal-to-kinetic energy conversion. However, krypton's low mass means, despite this, its thrust efficiency is < 0.01, instead of 0.15 for xenon. Importantly, iodine was found to have greater MN efficiency than xenon, producing thrust within 43$, showing it to be a viable low-cost alternative propellant.

Conservative estimates of iodine contamination on spacecraft surfaces yielded deposition rates of 0.32 mg/cm^2 over the standard REGULUS-50 operational life. How many particles react to or reflect off the surface will depend on the surface properties of the spacecraft, which is the next step in future development alongside plume-ambient plasma interactions [55]. Future work will also include coupling the 3D fluid model [39] to the PIC, instead of the GSM, which includes adding the capability for iodine chemistry in this solver. Finally, adding an RF power deposition model (instead of the assumption of constant η_{RF} used here) for the GSM will be explored. Lafleur et al. [32] have shown that the higher elastic scattering cross-sections in iodine lead to a higher collision frequency that favours the transfer of power between the electromagnetic fields of the RF antenna and the plasma. This may explain why the iodine model here generally

23

underestimated the experimental measures.

Acknowledgements

Appendix A. Performance metrics

The thrust F produced by the thruster discharge is given by [27]

$$F = F_0 + \iiint_V -j_{e\theta} B_r \ dV. \tag{A.1}$$

This is the volumetric integral of the product of azimuthal electron current density $j_{e\theta} = -en_e u_{e\theta}$ (calculated from integrating the moments of the PIC distribution) and the radial magnetic field B_r added to the source exit thrust $F_0 \approx 2n_{e0} k_B T_{e0} \pi \mathcal{R}^2$.

The thrust efficiency is then defined as

$$\eta_F = \frac{F^2}{2\dot{m} P_a} \tag{A.2}$$

The quality of the plasma production inside the source tube is measured with the mass utilisation efficiency and source production efficiency, which are, respectively,

$$\eta_u = \frac{\dot{m}_i}{\dot{m}}, \qquad \eta_s = \frac{P_*}{P_a} \tag{A.3}$$

The former is the percentage of propellent mass flow that is ionised; the latter is the ratio of the discharge exhaust power to the power absorbed from the RF antenna. The absorbed power is distributed via the exhaust, inelastic collisions and wall losses. Therefore, the source inefficiencies are

$$\varepsilon_{inel} = \frac{P_{inel}}{P_a}, \qquad \varepsilon_w = \frac{P_{wall}}{P_a} \tag{A.4}$$

which correspond to inelastic collision and wall losses. The performance of the magnetic nozzle is represented by the energy conversion and divergence efficiencies,

$$\eta_c = \frac{P_{iS}}{P_*}, \qquad \eta_d = \frac{P_{iS}^{(z)}}{P_{iS}} \tag{A.5}$$

which are the ratio of plume ion kinetic power to source tube exhaust power, and the percentage of that kinetic power in the axial direction respectively. The total MN efficiency is then $\eta_{MN} \approx \eta_c \eta_d$ and thrust efficiency is then given by $\eta_F \approx \eta_u \eta_s \eta_c \eta_d$ [35].

Table B.4: Thrust sensitivity analysis (REGULUS-150-Xe at $P_a = 150$ W)

Parameter/value	Thrust deviation [%]*
Bohm coefficient $\alpha_{\mathbf{B}}$	
<u>1/100</u>	0
1/64	-4.5
1/32	-20.0
1/16	-21.3
Background pressure [Pa]	
<u>10^{-5}</u>	0
10^{-4}	-0.1
10^{-3}	-1.32
10^{-2}	-13.63
SEE model	
100% absorption	-4.8
<u>h-BN</u>	0
90% secondary emission	+4.0

*From reference value (underlined) $\left(F - F_{ref}\right)/F_{ref}$

Appendix B. Sensitivity

There are several significant inputs to the PIC model that can greatly affect the plasma transport and resultant thrust. These are mainly: (i) the anomalous Bohm coefficient α_B; (ii) the background neutral density; and (iii) the secondary electron emission (SEE) coefficients/probabilities. While an informed choice can be made on these parameters (from empirical models, experimental background density measures or h-BN SEE models respectively), it is important to understand the sensitivity of their value on the experimental agreement.

Table B1 provides the thrust deviation from defined reference values for a single case of REGULUS-150-Xe at $P_a = 150$ W. Regarding α_B, there is a clear transition point between 1/64 and 1/32 where the thrust loss becomes $> 20\%$. This supports the presence of a critical hall parameter $\omega_{ce}/(\nu_B + \nu_e)$ required for adequate MN confinement [28]. Background pressure begins to have significant effect at $> 10^{-3}$ Pa, where $> 13\%$ deficit can be attributed to inelastic collision losses and reduced divergence efficiency from ion scattering. Finally, the SEE coefficients of Eqs. 8-11 were overridden to force 100% absorption and 90% secondary emission; this resulted in -4.8 and +4.0% thrust respectively compared to the empirical model of h-BN. Reduced electron absorption represents reduced wall power losses, while increased SEE will also cool the bulk plasma.

Provided that the choice of α_B is critical for the thrust estimate, it is worth further justifying the assumptions done in Section 3 regarding the value of this parameter. Under the theory of ion trapping saturation, the fluctuations in the azimuthal electric field and charged particle densities—that cause anomalous

25

transport—propagate in the $\mathbf{E} \times \mathbf{B}$ direction with a velocity close to the ion sound speed [56]. It may then be postulated that the equivalent Bohm-like collisionality scales with the plasma wave energy and associated instability frequency; that is $\alpha_B \propto \omega_{pi}/2\pi\sqrt{3}\omega_{ce}$ [56], where $\omega_{pi} = \sqrt{n_i e^2/\epsilon_0 m_i}$ is the ion plasma frequency. With pre-known PIC injection parameters at the inlet, the scaling was performed with ω_{pi*} and ω_{ce*}.

   Fig. B.1 illustrates this scaling for REGULUS-150-Xe, where the proportionality coefficient was selected to not exceed the fully-turbulent limit of 1/16 at high power. The sensitivity to α_B is further shown via the thrust curves for values of 1/100 and 1/16. For $P_{in} < 100$ W, α_B =1/100 clearly has the better agreement, remaining within the 25% error of measurements. However, up to 185 W, the thrust is overestimated by 48% and a value of 1/16 finds suitable agreement up to 150 W. Further work is necessary to establish a self-consistent model for anomalous collisionality.
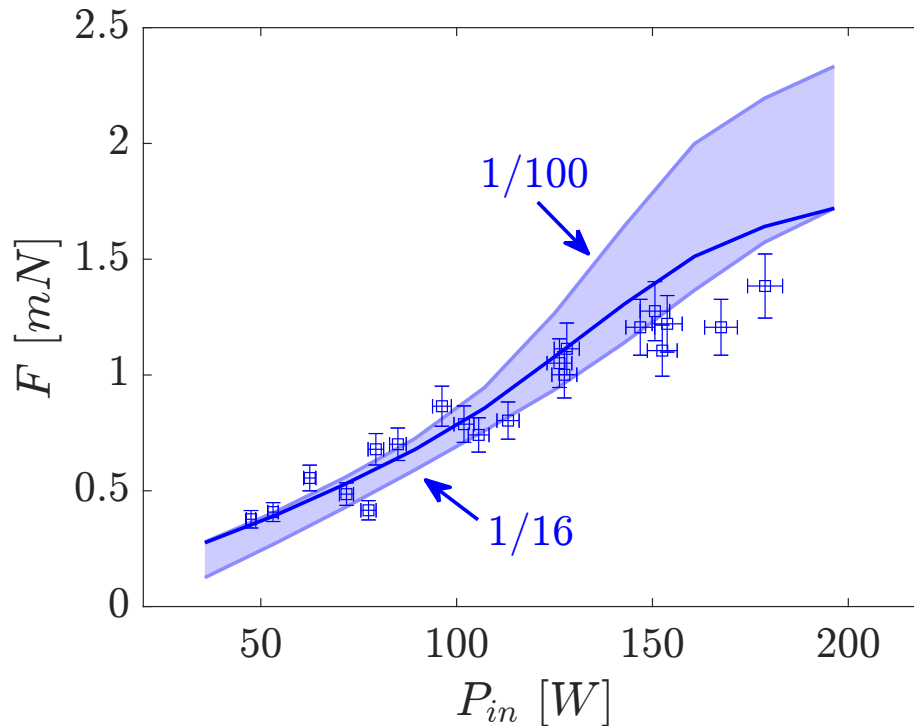

Figure B.1: Sensitivity of thrust to the Bohm coefficient for REGULUS-150-Xe.

References

[1] N. Koch, D. Pavarin, E. Ahedo, K. Katsonis, F. Scortecci, M. Pessana, Non conventional propellants for electric propulsion applications, in: Space Propulsion Conference, no. 1841086, San Sebastian, Spain, 2010.

[2] J. Muñoz Tejeda, A. Schwertheim, A. Knoll, Water as an environmentally friendly propellant for a multi-functional spacecraft architecture, in: Space Propulsion Conference, no. SP2022 0272, Estoril, Portugal, 2022.

[3] K. Holste, W. Gärtner, P. Köhler, P. Dietz, J. Konrad, S. Schippers, P. Klar, A. Müller, P. Schreiner, In search of alternative propellants for ion thrusters, in: 34th International Electric Propulsion Conference, no. 2015-320, Kobe, Japan, 2015.

[4] V. Giannetti, T. Andreussi, A. Leporini, S. Gregucci, A. Rossodivita, M. Andrenucci, D. Estublier, C. Edwards, M. M. Saravia, Electric propulsion sytem trade-off analysis based on alternative propellant selection, in: Space Propulsion Conference, Rome, Italy, 2016.

[5] A. Vinci, S. Mazouffre, Direct experimental comparison of krypton and xenon discharge properties in the magnetic nozzle of a helicon plasma source, Physics of Plasmas 28 (03 2021).

[6] J. Szabo, M. Robin, S. Paintal, B. Pote, V. Hruby, C. Freeman, Iodine propellant space propulsion, in: 33rd International Electric Propulsion Conference, no. 2013-311, The George Washington University, USA, 2013.

[7] N. Bellomo, M. Manente, F. Trezzolani, A. Gloder, A. Selmo, R. Mantellato, E. Toson, L. Cappellini, M. Duzzi, D. Scalzi, A. Schiavon, A. Barbato, D. Paulon, N. Souhair, M. Magarotto, M. Minute, R. Di Roberto, D. Pavarin, F. Graziani, Enhancement of microsatellites' mission capabilities: integration of regulus electric propulsion module into unisat-7, in: 70th International Astronautical Congress, no. IAC-19,C4,8-B4.5A,5,x52699, 2019.

[8] N. Souhair, et al., Simulation and modelling of an iodine fed helicon plasma thruster, in: 37th International Electric Propulsion Conference, no. IEPC-2022-496, Cambridge, USA, 2022.

[9] N. Greenwood, A. Earnshaw, Chemistry of the Elements, Butterworth-Heinemann, 1997.

[10] R. Dressler, Y.-H. Chiu, D. Levandier, Propellant alternatives for ion and hall effect thrusters, 2000.

[11] F. Cannat, T. Lafleur, J. Jarrige, P. Chabert, P.-Q. Elias, D. Packan, Optimization of a coaxial electron cyclotron resonance plasma thruster with an analytical model, Physics of Plasmas 22 (5) (2015) 053503.

[12] K. Takahashi, Helicon-type radiofrequency plasma thrusters and magnetic plasma nozzles, Reviews of Modern Plasma Physics 3 (1) (2019) 1–61.

[13] M. Manente, F. Trezzolani, M. Magarotto, E. Fantino, A. Selmo, N. Bellomo, E. Toson, D. Pavarin, Regulus: A propulsion platform to boost small satellite missions, Acta Astronautica 157 (2019) 241–249.

[14] C. Charles, R. Boswell, R. Laine, P. MacLellan, An experimental investigation of alternative propellants for the helicon double layer thruster, Journal of Physics D: Applied Physics 41 (2008) 175213. doi:10.1088/0022-3727/41/17/175213.

[15] D. Rafalskyi, J. Martínez Martínez, L. Habl, E. Zorzoli Rossi, P. Proynov, A. Boré, T. Baret, A. Poyet, T. Lafleur, S. Dudin, A. Aanesland, In-orbit demonstration of an iodine electric propulsion system, Nature 599 (2021) 411–415.

[16] N. Bellomo, M. Magarotto, M. Manente, et al., Design and in-orbit demonstration of regulus, an iodine electric propulsion system, CEAS Space Journal 14 (2022) 79–90.

[17] A. J. Sheppard, J. M. Little, Scaling laws for electrodeless plasma propulsion with water vapor propellant, Plasma Sources Science and Technology 29 (4) (2020) 045007.

[18] F. Romano, S. Fasoulas, T. Schönherr, N. Crisp, S. Haigh, R. Lyons, V. Oiko, P. Roberts, K. Smith, J. Becedas, G. Gonzales, I. Vazques, A. Brana, K. Antonini, K. Bay, L. Ghizoni, V. Jungnell, J. Morsbol, T. Binder, G. Herdrich, Performance evaluation of a novel inductive atmosphere-breathing ep system, in: 35th International Electric Propulsion Conference, no. IEPC-2017-184, Georgia, USA, 2017.

[19] K. Papavramidis, J. Skalden, N. Souhair, G. Herdrich, P. Maier, S. Klinkner, M. Fugmann, C. Traub, S. Fasoulas, F. Romano, Y.-A. Chan, P. Roberts, K. Smith, S. Edmondson, S. Haigh, N. Crisp, V. Oiko, L. Sinpetru, A. Macario-Rojas, B. Belkouchi, Development activities for the rf helicon-based plasma thruster: Thrust measurement and b-dot probe set-up, in: 37th International Electric Propulsion Conference, no. IEPC-2022-432, Boston, USA, 2022.

[20] N. Souhair, M. Magarotto, R. Andriulli, F. Ponti, Prediction of the propulsive performance of an atmosphere-breathing electric propulsion system on cathode-less plasma thruster, Aerospace 10 (2) (2023).

[21] P. Grondein, T. Lafleur, P. Chabert, A. Aanesland, Global model of an iodine gridded plasma thruster, Physics of Plasmas 23 (2016) 033514.

[22] K. Katsonis, C. Berenguer, A detailed global model of iodine plasma for optimization and diagnostics of electric thrusters, "Imperial Journal of Interdisciplinary Research (IJIR) 2 (11 2016).

[23] R. Lucken, et al., Global model of a magnetized ion thruster with xenon and iodine, in: 36th International Electric Propulsion Conference, no. IEPC-2019-678, Vienna, Austria, 2019.

[24] M. Magarotto, M. Manente, F. Trezzolani, D. Pavarin, Numerical model of a helicon plasma thruster, IEEE Transactions on Plasma Science 48 (4) (2020) 835–844.

[25] N. Souhair, M. Magarotto, F. Ponti, D. Pavarin, Analysis of the plasma transport in numerical simulations of helicon plasma thrusters, AIP Advances 11 (2021) 115016.

[26] E. Majorana, et al., Development of a plasma chemistry model for helicon plasma thruster analysis, Aerotec. Missili Spaz. 100 (2021) 225–238.

[27] M. Merino, J. Nuez, E. Ahedo, Fluid-kinetic model of a propulsive magnetic nozzle, Plasma Sources Science and Technology 30 (11) (2021) 115006.

[28] S. Andrews, S. D. Fede, M. Magarotto, Fully kinetic model of plasma expansion in a magnetic nozzle, Plasma Sources Science and Technology 31 (3) (2022) 035022.

[29] S. Di Fede, M. Magarotto, S. Andrews, D. Pavarin, Simulation of the plume of a magnetically enhanced plasma thruster with spis, Journal of Plasma Physics 87 (2021) 905870611.

[30] J. Zhou, D. Pérez-Grande, P. Fajardo, E. Ahedo, Numerical treatment of a magnetized electron fluid model within an electromagnetic plasma thruster simulation code, Plasma Sources Science and Technology 28 (11) (2019) 115004.

[31] N. Souhair, M. Magarotto, E. Majorana, F. Ponti, D. Pavarin, Development of a lumping methodology for the analysis of the excited states in plasma discharges operated with argon, neon, krypton, and xenon, Physics of Plasmas 28 (2021) 093504.

[32] T. Lafleur, L. Habl, E. Z. Rossi, D. Rafalskyi, Development and validation of an iodine plasma model for gridded ion thrusters, Plasma Sources Science and Technology 31 (11) (2022) 114001.

[33] M. Choi, Modeling an iodine hall thruster plume in the iodine satellite (isat), in: Joint Army-Navy-NASA-Air Force (JANNAF) 11th MSS / 9th LPS / 8th SPS / Joint Subcommittee Meeting, no. 20170001565, Cleveland, USA, 2016.

[34] I. Gomez, C. Toomer, Comparison and evaluation of numerical techniques and physico-chemical algorithms for the simulation of an iodine and xenon powered ion thrusters, The International Journal of Multiphysics 16 (2) (2022) 203–221.

[35] J. Zhou, F. Taccogna, P. Fajardo, E. Ahedo, Performance analysis of alternative propellants for a helicon plasma thruster, in: Space Propulsion 2020+1, no. SP2020 00191, 2021.

[36] M. Magarotto, S. Di Fede, N. Souhair, S. Andrews, M. Manente, F. Ponti, D. Pavarin, Numerical suite for magnetically enhanced plasma thrusters, in: 72nd International Astronautical Congress, no. IAC-20 C4.5.17, Virtual, 2020.

[37] M. Magarotto, S. Di Fede, N. Souhair, S. Andrews, F. Ponti, Numerical suite for cathodeless plasma thrusters, Acta Astronautica 197 (2022) 126–138.

[38] M. Guaita, M. Magarotto, M. Manente, D. Pavarin, M. Lavagna, Semi-analytical model of a helicon plasma thruster, IEEE Transactions on Plasma Science 50 (2022) 425–438.

[39] M. Magarotto, D. Melazzi, D. Pavarin, 3d-virtus: Equilibrium condition solver of radio-frequency magnetized plasma discharges for space applications, Computer Physics Communications 247 (2020) 106953.

[40] M. Magarotto, D. Pavarin, Parametric study of a cathode-less radio frequency thruster, IEEE Transactions on Plasma Science 48 (8) (2020) 2723–2735.

[41] M. Duzzi, M. Manente, F. Trezzolani, N. Bellomo, A. Barbato, L. Cappellini, M. Minute, R. Mantellato, M. Magarotto, D. Paulon, A. Schiavon, D. Scalzi, A. Selmo, E. Toson, F. Milza, L. Bianchi, D. Di Cara, D. Pavarin, E-regulus: development of a 150 w prototype of magnetically enhanced plasma thruster, in: 72nd International Astronautical Congress, no. IAC-21,C4,5,9,x65151, Dubai, United Arab Emirates, 2021.

[42] F. Marmuse, Iodine plasmas: experimental and numerical studies. application to electric propulsion, Ph.D. thesis, Paris, France (2020).

[43] L. Brieda, M. Keidar, Development of the starfish plasma simulation code and update on multiscale modeling of hall thrusters, in: 48th AIAA/ASME/SAE/ASEE Joint Propulsion Conference & Exhibit, no. AIAA 2012-4015, Atlanta, GA, USA, 2012.

[44] C. K. Birdsall, A. B. Langdon, Plasma physics via computer simulation, Tylor & Francis Group, New York NY, USA, 2005.

[45] K. Koura, Null-collision technique in the direct-simulation monte carlo method, The Physics of Fluids 29 (11) (1986) 3509–3511.

[46] A. Laturia, M. Van de Put, W. Vandenberghe, Dielectric properties of hexagonal boron nitride and transition metal dichalcogenides: from monolayer to bulk, npj 2D Materials and Applications 2 (03 2018).

[47] G. A. Bird, Molecular gas dynamics and the direct simulation of gas flows, Clarendon: Oxford University press, 1994.

[48] A. Dunaevsky, Y. Raitses, N. Fisch, Secondary electron emission from dielectric materials of a hall thruster with segmented electrodes, Physics of Plasmas 10 (2003) 2574–2577.

[49] D. Yu, F. Zhang, H. Liu, H. Li, G. Yan, J. Liu, Effect of electron temperature on dynamic characteristics of two-dimensional sheath in hall thrusters, Physics of Plasmas 15 (10) (2008) 104501.

[50] Y. V. Esipchuk, G. N. Tilinin, Drift instability in a hall-current plasma accelerator, Sov. Phys. - Tech. Phys. (Engl. Transl.); (United States) 21:4 (4 1976).

[51] E. Majorana, N. Souhair, F. Ponti, M. Magarotto, Development of a plasma chemistry model for helicon plasma thruster analysis (2021) 225–238.

[52] F. Trezzolani, M. Magarotto, M. Manente, D. Pavarin, Development of a counterbalanced pendulum thrust stand for electric propulsion, Measurement 122 (2018) 494–501.

[53] I. D. Kaganovich, A. Smolyakov, Y. Raitses, E. Ahedo, I. G. Mikellides, B. Jorns, F. Taccogna, R. Gueroult, S. Tsikata, A. Bourdon, J.-P. Boeuf, M. Keidar, A. T. Powis, M. Merino, M. Cappelli, K. Hara, J. A. Carlsson, N. J. Fisch, P. Chabert, I. Schweigert, T. Lafleur, K. Matyash, A. V. Khrabrov, R. W. Boswell, A. Fruchtman, Physics of e×b discharges relevant to plasma propulsion and similar technologies, Physics of Plasmas 27 (12) (2020) 120601.

[54] N. Bellomo, et al., Regulus electric propulsion system integration in unisat-7 microsatellite and in a 6 unit cubesat for iod and tests, in: 71st International Astronautical Congress, no. IAC-21 C4.6.3, Dubai, UAE, 2021.

[55] Characterising satellite aerodynamics in very low earth orbit inclusive of ion thruster plume-thermosphere/ionosphere interactions, Acta Astronautica 170 (2020) 386–396.

[56] V. Croes, T. Lafleur, et al., 2d particle-in-cell simulations of the electron drift instability and associated anomalous electron transport in hall-effect thrusters, Plasma Sources Science and Technology 26 (2017) 034001.